optica

Deep-tissue label-free quantitative optical tomography: supplement

JELLE VAN DER HORST, ANNA K. TRULL, AND JEROEN KALKMAN*

Department of Imaging Physics, Delft University of Technology, Lorentzweg 1, 2628 CJ Delft, The Netherlands
Corresponding author: j.kalkman@tudelft.nl

Deep-tissue label-free quantitative optical tomography: supplementary material

JELLE VAN DER HORST[1], ANNA K. TRULL[1], AND JEROEN KALKMAN[1]

[1]*Department of Imaging Physics, Delft University of Technology, Lorentzweg 1, 2628 CJ Delft, The Netherlands*
[*]*Corresponding author: j.kalkman@tudelft.nl*

Compiled November 18, 2020

This document provides supplementary information to "Deep-tissue label-free quantitative optical tomography," https://doi.org/10.1364/OPTICA.397549. This supplement describes the experimental set-up, sample preparation, analysis of OCPT resolution, calibration for quantitative imaging, and zebrafish tissue optical properties in more detail.

---

1. OCPT EXPERIMENTAL SETUP

The optical coherence projection tomography (OCPT) setup is a fiber-based transmission spectral-domain low-coherence interferometry setup, as shown in Fig. 1(a) of the manuscript, and, in more detail, in Fig. S1.

Light from a super-luminescent diode (D-1300-HP, Superlum), with a center wavelength of 1300 nm and a bandwidth of 110 nm is coupled into a Mach-Zehnder interferometer based on two 90/10 fiber-optic couplers (TW1300R2A2, Thorlabs).

In the sample arm light is focused onto the sample with a 54 mm focal distance lens (LSM54-1310, Thorlabs), where it interacts with the measured object before being collimated with a second lens. The focal spot between the two lenses is scanned and subsequently de-scanned rapidly in the lateral, t, direction by a pair of galvo scanning mirrors (Rhothor deflector RTA-AR180, Newson) placed in the back focal plane of both lenses, creating a telecentric scanning system. After collimation by the second lens and de-scanning by the second scanning mirror the beam is coupled back into the single mode fiber and recombined with the reference arm. Detection is performed using a home build spectrometer based on a holographic grating (1145 l/mm, Wasatch Photonics), an SWIR imaging lens (S5LPJ0037/360, Sill Optics), and a 76 kHz InGaAs linescan camera (GL2048L, Sensors Unlimited). An optical amplifier (BOA11323S, Thorlabs) is placed in the sample arm to increase the optical power on the sample to a maximum of 100 mW. The polarisation of both arms is controlled using two fiber polarisation controllers (FPC560, Thorlabs). The spectrometer data is transferred to the computer via a framegrabber (PCIe-1433, National Instruments). The spectrometer camera is triggered by the controller of the scanning mirrors and the entire system is operated by custom Labview software. The transmission optical coherence tomography (OCT) setup has a lateral full width at half maximum (FWHM) reso-lution of 20 µm measured in water at the center of the field of view (FOV), a sensitivity of -116 dB and an axial resolution of 29 µm (in air). The sample is rotated and translated vertically with a motorized sample holder to obtain projection data of the entire object under different angles and vertical positions, as required for tomographic reconstruction of multiple slices of the measured object.

The motorised sample holder consist of 3 linear stepper motors (8MT167-25LS, Standa) and a stepper motor for rotation (8MR151-30, Standa). The stepper motor stage assembly is controlled using a 4 axis stage controller (Tango Desktop, Märzhäuser). A sample is mounted right below the rotation stage using a 16 mm cage system that provides manual tip-tilt and x, y translation for fine alignment of the sample with respect to the rotation axis. The system is aligned so that the center of rotation coincides with the focal point of the sample arm lenses and with the center of the sample. The sample is glued to the cage system and immersed into a $10 \times 50 \times 50$ optical glass cuvette (HELL700000-10-10, VWR) filled with a refractive index matched fluid to reduce refraction effects.

2. OCPT SCANNING TRANSMISSION SAMPLE ARM

The scanning mirrors in the telecentric system are controlled by separate controllers (CUA32, Newson Belgium) that are linked together and synchronized in a master slave system. Both mirrors are connected using 50 cm coaxial cables. Imperfections in the alignment of the scanning system cause errors in de-scanning of the beam and therefore power loss when the light is coupled back into the single mode fiber. This is solved by the implementation of an algorithm that optimizes the scanning motion of the de-scanning mirror for maximum power transmission over the scanning range of the mirrors. The result of the standard and optimized scan condition is shown in Fig. S2. The focal spot is
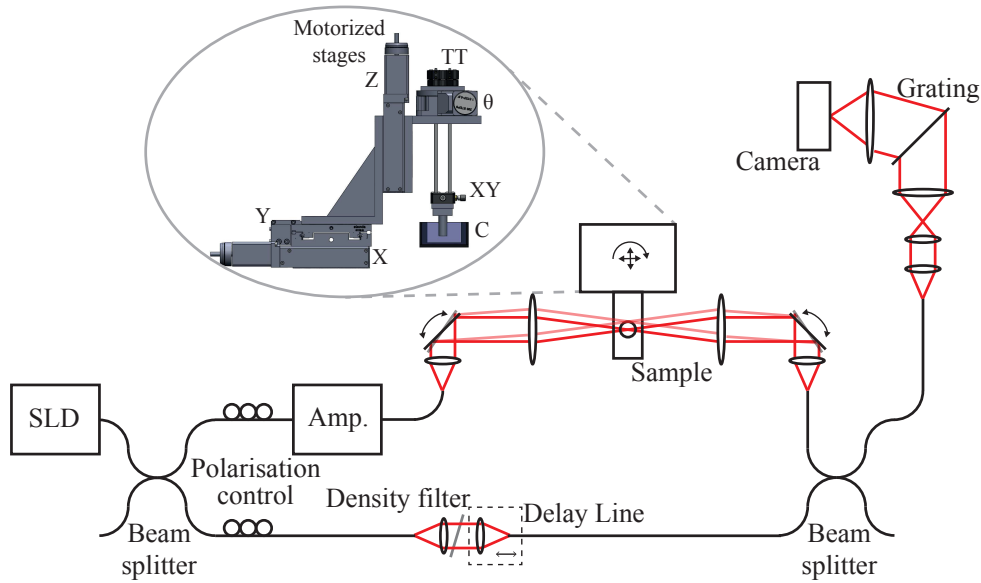
Fig. S1. Schematic representation of the OCPT setup.

scanned ±4 mm from its center position at an average speed of 400 mm/s with a frequency of 25 Hz. No scan velocity dependent behaviour of the power transmission is observed in the implemented scan velocity range. The focal spot in the center of the scan range is approximately 20 µm (FWHM) and increasing towards the edges, i.e. in the scanning geometry the resolution is not shift invariant.
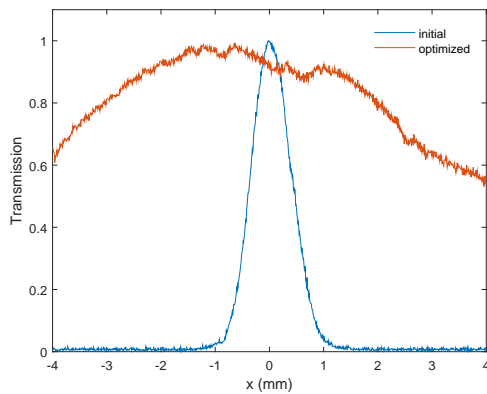

Fig. S2. Power transmission of OCPT sample arm. Optical power as a function of lateral coordinate for a non-optimized (blue) and optimized (red) scanning motion of the de-scan galvo mirror.

3. SAMPLE PREPARATION AND IMAGING

A. Scattering phantom

Silicone phantoms were created by mixing and curing Sylgard (Sylgard 184 elastomer kit, Dow Corning) in a cylindrical container. Before curing, titanium dioxide (Titanium(IV) oxide anatase, Aldrich) was added to the solution to create scattering centers in the material. The sample was immersed in a cuvette filled with index-matching 48% sugar water solution to minimize refraction along the light path. The phantom material was measured in 64 transverse slices spaced 8 µm apart. Each slice was measured with 1000 lateral sampling points covering 8 mm, and 180 angular projections with a sampling distance of 1°. In the angular direction, the acquisition was undersampled to limit the total acquisition time.

B. Attenuation calibration phantom

Validation measurements of the quantitative image contrast were performed using a 2% low-melting point agarose (VWR International b.v.) cylinder immersed in dilutions of Intralipid with water (Intralipid 20%, Fresenius Kabi). For each concentration, 1 transverse slice was reconstructed using 1000 lateral measurements covering 8 mm and 180 angular projections with a 1° spacing. The optical properties were determined by averaging a region of interest of 100 by 100 pixels. The results were compared with single-transmission OCT measurements of the bulk Intralipid-water mixtures and the agarose.

C. Zebrafish sample

Experiments were performed on adult zebrafish mounted in 2% low-melting point agarose gel. Before fixation in agarose, the zebrafish were euthanized in ice water in the Erasmus University Medical Centre Rotterdam (Erasmus MC) according to animal welfare regulations. Animal experiments were approved by the Animal Experimentation Committee of the Erasmus MC. The agarose was encased in tube of 4 mm inner diameter. The tube was made of fluorinated ethylene propylene (FEP), which has a refractive index close to that of water. The FEP tube containing the agarose and the zebrafish was attached to the sample holder assembly. The zebrafish sample was immersed in a cuvette filled with water to minimize differences in refractive index along the light path. A total of 200 transverse slices were recorded, homogeneously spaced over a 20 mm range. The lateral and angular sampling was the same as presented for the phantom experiments. The 3D volume was acquired in 24 minutes during which 137 GB of raw data was acquired.

4. OCPT DATA PROCESSING AND IMAGE RECONSTRUCTION

After acquisition the experimental data is stored in raw binary format. Data is processed using software written in MATLAB (Mathworks, R2014b). The data analysis steps are depicted in Fig. 1(a-d). The transmission OCT signal as a function of optical path length is calculated from the recorded spectra using standard OCT signal processing [1, 2]. The background spectrum of the reference arm is subtracted from the measured interference signal and the resulting spectrum is corrected for dispersion mismatch and nonlinear sampling of the spectrum in the spectrometer [3]. Finally, the optical path length distribution (OPLD) is calculated by taking the absolute value of the inverse Fourier transform of the corrected spectrum.

Scattered light is suppressed in the data analysis by selecting only early arriving photons from the OPLD. The first rising edge in the OPLD is detected by locating the first value higher than three times the standard deviation σ of the noise floor in a region of interest, as shown in Fig. S3(c). The region of interest is set prior to the analysis based on the size and estimated refractive index of the sample. A fit with a Gaussian function is initialized with 10 pixels around the rising edge. The location and height of the fitted Gaussians are used as measures for the path-length-integrated group refractive index and the total attenuation accumulated along the ballistic light path [1, 2].

The large difference in light transmission T between the immersion fluid ($T \approx \mathrm{e}^{-1}$) and a highly scattering object ($T \approx \mathrm{e}^{-25}$) requires a high dynamic range of the detection setup. Due to the limited dynamic range of the OCPT hardware (38 dB) the setup is optimised for the detection of the small signals originating from the sample. Therefore the spectrometer is saturated when sampling the immersion fluid surrounding and edge regions of the object. Spectrometer saturation is detected in the interference spectra and the corresponding sinogram pixels are set to the values corresponding to the immersion fluid, obtained by separate measurements with the appropriate dynamic range settings.

The calculated path-length-integrated attenuation coefficient and group refractive index are placed in two separate sinograms $p_{\mu_t}(\theta, t)$ and $p_{n_g}(\theta, t)$ using

$$p_{\mu_t}(\theta, t) = \int \Delta\mu_t(s\sin(\theta) + t\cos(\theta), -s\cos(\theta) + t\sin(\theta))\mathrm{d}s \tag{S1}$$

$$= \int \Delta\hat{\mu}_t(s, t)\mathrm{d}s = 2\ln\left(\frac{a(t)_{ref}}{a(\theta, t)_{samp}}\right), \tag{S2}$$

$$p_{n_g}(\theta, t) = \int \Delta n_g(s\sin(\theta) + t\cos(\theta), -s\cos(\theta) + t\sin(\theta))\mathrm{d}s \tag{S3}$$

$$\int \Delta\hat{n}_g(s, t)\mathrm{d}s = b(\theta, t)_{samp} - b(t)_{ref} \tag{S4}$$

Where s is the direction along the ray path, t the lateral coordinate, θ the projection angle, $a(\theta, t)_{samp}$ is the peak height determined from a Gaussian fit, $b(\theta, t)_{samp}$ is the location of the detected peak, and $a(t)_{ref}$ and $b(t)_{ref}$ are reference curves representing, respectively the absolute sample arm transmission and optical path-length dependence on lateral position. These curves are obtained by performing a reference lateral sweep measurement of a cuvette filled with immersion fluid. The variable $\hat{\mu}_t(s, t)$ $\hat{n}_g(s, t)$ describe $\Delta\mu_t(x, y)$ and $\Delta n_g(x, y)$ in the coordinate frame of the projection.

The problem of reconstructing images from the collection of path-length-integrated values $p_{\mu_t}(\theta, t)$ and $p_{n_g}(\theta, t)$ is the same as for X-ray computed tomography, provided that the depth of field of the transmission OCT system is comparable or larger than the object size [4]. Initially, the sinograms are filtered to remove outliers that cause streak artifacts in the reconstructed images. When a sinogram pixel deviates more than 15% from the average of its 8 surrounding pixels it is replaced by the median value of these surrounding pixels. After correction of the sinograms for center of rotation offsets, quantitative images of the optical properties relative to the index-matching fluid are reconstructed using filtered backprojection (FBP) or the algebraic reconstruction technique (ART) [5]. The ART reconstruction uses a randomised projection order, and executes 4 iterations over all the projections. During the ART reconstruction of the attenuation image a positivity constraint is imposed on the solution. Reconstruction using ART takes approximately 18 seconds per slice. Finally, the absolute value of the group refractive indices and attenuation coefficients are calculated by adding an offset from a reference transmission OCT measurement of the surrounding medium. Visualisations in 3D are created using an intensity threshold and opacity settings in Drishti software package [6].

By applying different data analysis steps to the same OCPT data set three different reconstructions can be obtained: a confocal gated attenuation image, a confocal plus coherence gated attenuation image, and an OCPT attenuation image. With this we can the study of the improvements achieved by the separate gating techniques.

From the transmission OCT spectrum $S_\theta(k_j, t)$ the confocal only transmission signal is determined by subtraction of the reference arm spectrum S_{ref} and integration of the remaining intensity (the interference contribution cancels). From this transmission signal the projections of the attenuation are determined and a tomographic image is reconstructed with ART. The confocal only sinogram is given by

$$p_{\mu_t,\mathrm{conf}}(\theta, t) = \ln\left(\frac{\sum S_{\mathrm{bg}}(k_j, t)}{\sum S_\theta(k_j, t) - \sum S_{\mathrm{ref}}(k_j)}\right), \tag{S5}$$

where $S_{\mathrm{bg}}(k_j, t)$ is the t dependent sample arm transmission spectrum of the background (index-matching) medium. Reference arm and sample arm spectra are recorded separately by blocking of the opposite interferometer arm. The sum in Eq. S5 extends over all pixels j of the spectrometer and effectively filters out the high frequency interference signal from the remaining sample arm transmission spectrum, as shown in Fig. S3(a). The sinogram $p_{\mu_t,\mathrm{conf}}(\theta, t)$ is reconstructed in the same way as the OCPT sinograms. As the confocal gated reconstructed image is created without making use of the interference signal, this image does not profit from the heterodyne detection, the coherence gate, nor the time gate.

A confocal and interference gated attenuation image is made by integrating the OPLDs over a region of 2 mm, which starts right before the ballistic signal, as shown in Fig. S3(b). The confocal and inteference gated sinogram is computed using

$$p_{\mu_t,\mathrm{conf+coh}}(\theta, t) = 2\ln\left(\frac{\sum |a(t)_{ref,i}|}{\sum |a(\theta, t)_{samp,i}|}\right), \tag{S6}$$

where the sum is taken over the pixels i in the OPLD in the described 2 mm region. Again, tomographic images are reconstructed in the same manner as before. Light detected in each pixel on the spectrometer that relative to the reference beam has a changed its polarization, or is not coherent within the coherence length of a single pixel, will contribute to the background
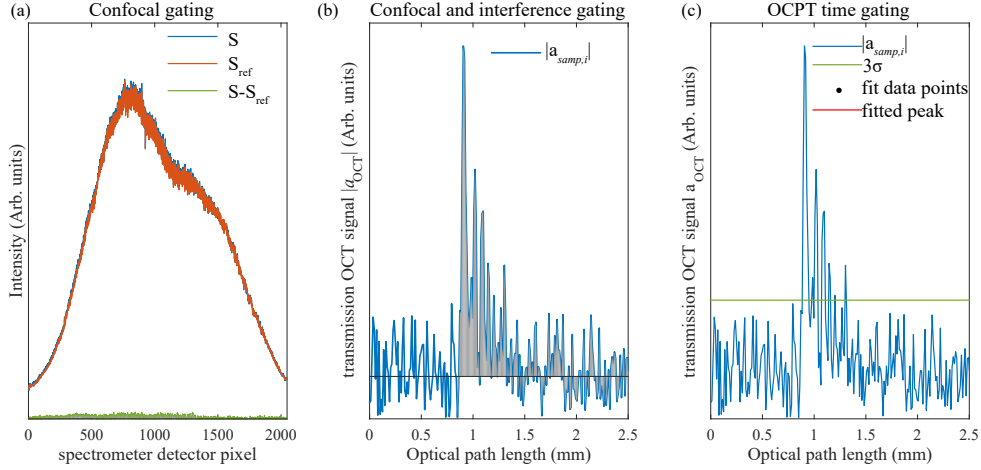
Fig. S3. Overview of the different gating methods. (a) Confocal gated tomographic images are created by integration of the shown spectra. (b) Confocal and interference gated tomographic images are created by integration of interference signal in the spatial domain. (c) OPLD time gated images are obtained by fitting a single peak in the spatial domain.

signal in the spectrum and does not contribute to the interference pattern and the tomographic image.

5. OCPT QUANTITATIVE IMAGING

The quantitative determination of optical material properties of $\Delta\mu_t$ and Δn_g is validated using tissue phantoms. Figure S4 shows the material properties determined in an agarose cylinder filled with Intralipid. The values obtained with OCPT agree well with the values obtained with a reference measurement.

6. OCPT IMAGE RESOLUTION

The spatial resolution of the OCPT system depends on the entire through focus point spread function (PSF) of the confocal lens system and in general is a function of distance from the center of rotation. In our measurements, the optical focus coincides with the center of rotation. Hence, objects at the center of rotation are in focus for every projection angle creating an isotropic image PSF with a FWHM size equal to the beam waist in focus. Objects at locations s away from the center of rotation are periodically in focus and out of focus depending on the projection angle. For these locations the image PSF is elongated in the tangential direction.

For optical projection tomography (OPT) the resolution in the tangential and radial direction is described by the 2D model [4]. For a focused Gaussian beam the intensity distribution $I(r,s)$ is

$$I(r,s) = \frac{2}{\pi w^2(s)} \exp\left(-\frac{2r^2}{w^2(s)}\right), \qquad (S7)$$

where r is the radial distance from the optical axis, and $w(s)$ is the beam waist through focus at a distance s from the axis of rotation, given by

$$w(s) = \sqrt{w_0^2 + \frac{\lambda^2 s^2}{\pi^2 w_0^2}}, \qquad (S8)$$

with λ the emission wavelength of the fluorophore and w_0 the Gaussian beam waist defined as the e^{-1} value of the field amplitude in focus [7].

In OPT, the spatial PSF in the tomographic images caused by the imaging optics is given by

$$PSF(u,v) = \sqrt{\frac{1}{\pi^2 a_u a_v}} \exp\left(-\left[\frac{u^2}{a_u} + \frac{v^2}{a_v}\right]\right). \qquad (S9)$$

where (u,v) is a rotated and translated coordinate system, as shown in Fig S5(a), with axes along the local radial (u) and tangential (v) directions. The Gaussian widths $a_u = w^2(0)/2$ and $a_v = w^2(s)$ are related to the through focus beam waist $w(s)$. For every object position (x_o, y_o) in the image (u,v) is given by

$$\begin{bmatrix} u \\ v \end{bmatrix} = \begin{bmatrix} \cos(-\theta_o) & -\sin(-\theta_o) \\ \sin(-\theta_o) & \cos(-\theta_o) \end{bmatrix} \begin{bmatrix} x - x_o \\ y - y_o \end{bmatrix}, \qquad (S10)$$

where $\theta_o = \tan^{-1} y_0/x_0$.

However, in OCPT, the sinograms are pre-processed using Eq. S2 and S4 before reconstruction, causing a change in the resolution of the processed sinograms compared to an OPT system with the same optical system. Consequently, the image resolution in the reconstructed tomographic images differs between an OCPT and an OPT system using the same optical system. Here, we process both the reference measurement of $I(r,s)$ and the tomographic experimental data in the same way to determine the accuracy of the model for OCPT. In addition, OCPT differs from OPT because of the inhomogeneity of the resolution across the scan range of the imaging setup causing the system to not be linear shift invariant. This prohibits a similar straightforward analysis of the image resolution for OCPT.

The spatial resolution in OCPT is measured using a silicone phantom doped with titanium dioxide. First, the PSF $I(r,s)$ of the confocal lens system is measured at several positions from focus using a knife edge. Second, the through-focus FWHM of the beam waist is determined after performing the processing required for the OCPT, described in Eq. S2. In the tomographic image, clusters of titanium dioxide in the 3D volume are located and fitted with a bivariate Gaussian model in every slice (x,y) across the volume. The vertical resolution is determined separately using a 1-dimensional Gaussian fit. The FWHM spotsizes in the radial, tangential and vertical directions are determined from the Gaussian fits. The resolution is investigates in two
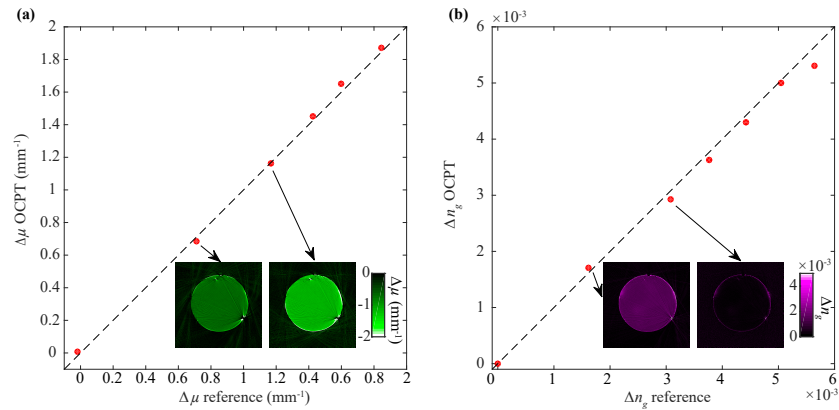
Fig. S4. OCPT quantitative imaging. The attenuation coefficient (a) and group refractive index (b) determined from the tomographic OCPT images versus their corresponding reference values measured with transmission OCT. Errors associated with measurements are smaller than the marker size.
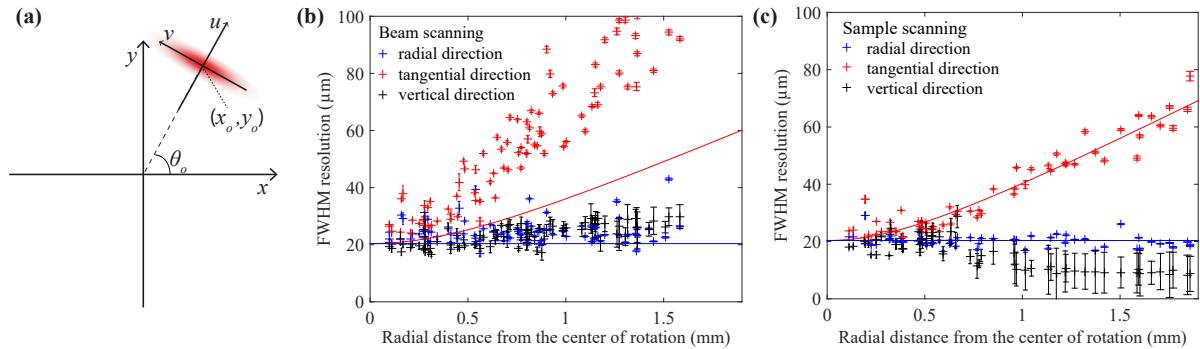

Fig. S5. OCPT spatial resolution analysis. (a) Definition of coordinate systems in the image plane. (b) Beam scanning FWHM resolution in the radial (blue points), tangential (red points), and vertical (black points) direction as a function of the radial distance from the center of rotation. Error bars indicate 95% confidence intervals. (c) Sample scanning resolution analysis. For both cases the in-focus beam waist (blue line) and through-focus beam waist (red line) predicting the radial and tangential resolutions for sample scanning are plotted for comparison.

conditions, either with sample scanning or with beam scanning, and the analysis is shown in Fig. S5(b) and (c). In the the first case the PSF is shift invariant, in the second case it is not. In both cases the resolution in the radial direction is constant across the imaged volume and equal to the in-focus beam waist of the confocal lens system. The resolution in the tangential direction increases with the radial distance from the center of rotation following the through-focus beam waist of the lens system.

For the shift variant sample arm scanning the resolution deteriorates faster than for the sample scanning imaging. We attribute this to poorer resolution at the edges of the scan range where the resolution of the imaging system is slightly worse. Fitting the tangential and radial spotsizes for the beam scanning with the 2D OPT model turns out to be impossible. For sample scanning, fitting the measured tangential and radial FWHM spotsizes with the 2D OPT model from Eq. S9 gives $w_0 = (17.33 \pm 0.42)$ µm and $\lambda = (1613 \pm 120)$ nm. This is consistent with the parameters obtained from a separate knife-edge measurement of the optical beam profile in the index-matching fluid processed similar as OCPT: $w_0 = (14.92 \pm 3.17)$ µm and $\lambda = (1272 \pm 339)$ nm. While the model does not describe the physical µ-PSF and the fit parameters do not describe the physical light intensity distribution in the sample arm confocal imaging system, the model fits well and shows the consistency of the knife edge measurement with the measured image resolution.

7. QUANTITATIVE OCPT IMAGING OF ZEBRAFISH TISSUE PROPERTIES

The segmentation of the zebrafish organs is based on the assumption that neighbouring pixels have a similar attenuation coefficient and/or refractive index. The zebrafish organs are segmented using several standard methods, applied to either the refractive index image, the attenuation image or to both images. The segmentation of the skin surface is performed by thresholding the attenuation image using the threshold $\mu_t = 5$ mm^{-1} and successive image erosion, dilation and filling of closed holes in the binary image. The swim bladder is segmented by thresholding the refractive index image using the threshold $n_g = 1.000$. The eye lens is segmented by thresholding the refractive index image using the threshold $n_g = 1.400$. The brain is segmented by hand. The spine is segmented with a threshold of $\mu_t = 11$ mm^{-1}. For the estimation of the optical properties, the MATLAB build-in function *median* was used. The surface area is determined from the segmented images using application of a surface area metric [13]. The volumes are determined by summation of the segmented pixel numbers multiplied by the voxel volume of 6.4 pL.

Table S1 gives an overview of quantitative OCPT imaging of zebrafish tissue properties. For various zebrafish organs the organ surface area, volume, median attenuation coefficient, and

Table S1. Zebrafish tissue optical properties and organ sizes measured with OCPT. Surface area (A), Volume (V), median attenuation (μ_t), and median group refractive index (n_g) values obtained using segmented OCPT measurements compared with literature values. gm: Gray matter, wm: white matter, thala: thalamus.

Organ	A (mm^2)	V (µL)	μ_t (mm^{-1})	Lit. value μ_t (mm^{-1})	n_g	Lit. value n_g
Brain	9.0	1.56	5.197 ± 0.008	gm: 5 ± 3 [8] wm: 10 ± 2 [8] thala: 8 ± 3 [8]	1.3569 ± 0.0001	1.41 ± 0.02 [9]
Lens	2.6	0.16	9.72 ± 0.06	7 to 9 [10]	1.4556 ± 0.0007	1.55 ± 0.02 [11]
Spine	10.3	0.62	16.19 ± 0.02	spinal fluid 5 ± 0.7 [8]	1.3664 ± 0.0002	-
Swim bladder	18.0	1.08	4.17 ± 0.04	0	0.903 ± 0.001	1 [12]
Zebrafish	136 .4	51.48	-	-	-	-

median group refractive index values are quantified. The stated uncertainties are standard deviations of the mean calculated over the pixels in the particular organ. The obtained parameters are compared with literature values of similar tissues from other organisms measured with different methods, as far as available. Overall, the zebrafish organ attenuation coefficients are in good agreement with the values found in literature. The segmented brain is a mixture of grey matter, white matter, and thalamus and the attenuation coefficient is a weighted average of the attenuation coefficients of these tissues. The attenuation of the lens is in a good agreement with the literature value. The attenuation value of the spine is slightly higher compared to the literature value for spinal fluid. The difference is attributed to the inclusion of spinal bone, which is expected to raise the attenuation coefficient. In the swim bladder, we expect an attenuation of 0 mm^{-1}. The elevated value of the attenuation coefficient occurs primarily in the center of the swim bladder, which we attribute to image artefacts due to refraction at the swim bladder interface.

The group refractive index values are in good agreement with values reported in literature. The literature value of the refractive index for the lens [11] was measured at 800 nm. Considering typical dispersive properties of tissue we expect this wavelength dependence to only give deviations of the order of $\Delta n_g \approx 0.03$ for a wavelength of 800 nm compared to the measured value at 1300 nm [14]. The refractive index of the swim bladder and brain tissue was reported at the wavelength of 1300 nm [9, 12].

REFERENCES

1. V. D. Nguyen, D. J. Faber, E. van der Pol, T. G. van Leeuwen, and J. Kalkman, "Dependent and multiple scattering in transmission and backscattering optical coherence tomography," Opt. Express **21**, 29145 (2013).
2. A. K. Trull, J. van der Horst, J. G. Bijster, and J. Kalkman, "Transmission optical coherence tomography based measurement of optical material properties," Opt. Express **23**, 33550 (2015).
3. A. F. Fercher, C. K. Hitzenberger, M. Sticker, R. Zawadzki, B. Karamata, and T. Lasser, "Numerical dispersion compensation for partial coherence interferometry and optical coherence tomography," Opt. Express **9**, 610 (2001).
4. J. van der Horst and J. Kalkman, "Image resolution and deconvolution in optical tomography," Opt. Express **24**, 24460 (2016).
5. A. C. Kak and M. Slaney, *Principles of computerized tomographic imaging* (SIAM, 2001).
6. A. Limaye, "Drishti: a volume exploration and presentation tool," in *Developments in X-Ray Tomography Viii*, vol. 8506 (International Society for Optics and Photonics, 2012), p. 85060X.
7. H. Kogelnik and T. Li, "Laser beams and resonators," Proc. IEEE **54**, 1312–1329 (1966).
8. V. Tuchin, *Tissue optics: light scattering methods and instruments for medical diagnosis* (SPIE press Bellingham, 2007).
9. J. Sun, S. J. Lee, L. Wu, M. Sarntinoranont, and H. Xie, "Refractive index measurement of acute rat brain tissue slices using optical coherence tomography," Opt. Express p. 1084 (2012).
10. R. L. Vincelette, A. J. Welch, R. J. Thomas, B. Rockwell, and D. J. Lund, "Thermal lensing in ocular media exposed to continuous-wave near-infrared radiation: The 1150-1350-nm region," J. Biomed. Opt. **13**, 054005 (2008).
11. L. Garner, G. Smith, S. Yao, and R. Augusteyn, "Gradient refractive index of the crystalline lens of the black oreo dory (allocyttus niger): comparison of magnetic resonance imaging (MRI) and laser ray-trace methods," Vis. Res. **41**, 973 (2001).
12. P. E. Ciddor, "Refractive index of air: new equations for the visible and near infrared," Appl. Opt. **35**, 1566 (1996).
13. D. Legland, K. Kiêu, and M.-F. Devaux, "Computation of minkowski measures on 2d and 3d binary images," Image Analysis & Stereol. **26** (2011).
14. H. Ding, J. Q. Lu, W. A. Wooden, P. J. Kragel, and X.-H. Hu, "Refractive indices of human skin tissues at eight wavelengths and estimated dispersion relations between 300 and 1600 nm," Phys. Med. Biol. **51**, 1479 (2006).